# Quasi-static granular flow of ice mélange

J. M. Amundson and J. C. Burton

Originally published in: Amundson, J. M., & Burton, J. C. (2018). Quasi-static granular flow of ice mélange. Journal of Geophysical Research: Earth Surface, 123. https://doi.org/10.1029/2018JF004685

ADVANCING EARTH AND SPACE SCIENCE

JGR

Journal of Geophysical Research: Earth Surface

RESEARCH ARTICLE

10.1029/2018JF004685

**Key Points:**

- Ice mélange velocity fields can be uniform, compressional, or extensional
- Winter velocity fields are approximated by quasi-static granular flow
- Velocity profiles are consistent with viscoplastic rheologies for granular materials

**Supporting Information:**

- Supporting Information S1
- Data Set S1

**Correspondence to:**
J. M. Amundson,
jmamundson@alaska.edu

**Citation:**
Amundson, J. M., & Burton, J. C. (2018). Quasi-static granular flow of ice mélange. *Journal of Geophysical Research: Earth Surface*, *123*. https://doi.org/10.1029/2018JF004685

Received 2 APR 2018
Accepted 29 AUG 2018
Accepted article online 11 SEP 2018

# Quasi-Static Granular Flow of Ice Mélange

**J. M. Amundson**[1,2] and **J. C. Burton**[3]

[1]Department of Natural Sciences, University of Alaska Southeast, Juneau, AK, USA, [2]Institute for Atmospheric and Earth System Research, University of Helsinki, Helsinki, Finland, [3]Department of Physics, Emory University, Atlanta, GA, USA

**Abstract** We use Landsat 8 imagery to generate ice mélange velocity fields at Greenland's three most productive outlet glaciers: Jakobshavn Isbræ, Helheim Glacier, and Kangerdlugssuaq Glacier. Winter velocity fields are generally steady and highly uniform. Summer velocity fields, on the other hand, tend to be much more variable and can be uniform, compressional, or extensional. We rarely observe compressional flow at Jakobshavn Isbræ or extensional flow at Helheim Glacier, while both are observed at Kangerdlugssuaq Glacier. Transverse velocity profiles from all three locations are suggestive of viscoplastic flow, in which deformation occurs primarily in shear zones along the fjord walls. We analyze the transverse profiles in the context of quasi-static flow using continuum rheologies for granular materials and find that the force per unit width that ice mélange exerts on glacier termini increases exponentially with the ice mélange length-to-width ratio and the effective coefficient of friction. Our estimates of ice mélange resistance are consistent with other independent estimates and suggest that ice mélange may be capable of inhibiting iceberg calving events, especially during winter. Moreover, our results provide geophysical-scale support for constitutive relationships for granular materials and suggest a potential avenue for modeling ice mélange dynamics with continuum models.

## 1. Introduction

The stability of marine-terminating outlet glaciers is strongly affected by processes occurring at or near the ice-ocean interface. For these glaciers, the rate of change of glacier length is given by

$$\frac{\mathrm{d}L_g}{\mathrm{d}t} = U_t - U_f, \tag{1}$$

where $L_g$ is the glacier length, $U_t$ is the terminus velocity, and $U_f$ is the frontal ablation rate (sum of iceberg calving and submarine melting). Due to the highly nonlinear behavior of ice flow, small changes in ice velocity or the frontal ablation rate can lead to sustained, runaway retreat. For example, terminus retreat into deep water or past a constriction results in a loss of flow resistance, which promotes thinning, flow acceleration, and an increase in calving activity. This instability can lead to 10's of kilometers of retreat over several decades (e.g., Pfeffer, 2007; Post et al., 2011).

Seasonal variations in terminus position, which occur due to variations in both ice flow and frontal ablation, likely affect secular variations in glacier dynamics by influencing the mean annual ice thickness near a glacier's terminus (Amundson & Truffer, 2010; Joughin et al., 2012). Several studies have correlated seasonal advance and retreat cycles of glaciers in Greenland to variations in the strength of proglacial ice mélange (Amundson et al., 2010; Cassotto et al., 2015; Howat et al., 2010; Joughin et al., 2008), a heterogeneous granular material composed of icebergs and sea ice. In some cases (e.g., Figure 1), calving completely ceases during winter and only resumes after the sea ice and ice mélange lose structural rigidity.

A simple force balance analysis suggests that the resistive stress from ice mélange does not need to be large relative to other glaciological stresses in order to influence calving (Amundson et al., 2010). Field data (Walter et al., 2012) and discrete element models (Burton et al., 2018; Robel, 2017) indicate that resistive stresses in ice mélange may indeed be sufficiently high to inhibit calving, although it is also clear that the resistive stresses vary temporally and between fjords (Cassotto et al., 2015; Fried et al., 2018; Moon et al., 2015). Resistance from ice mélange likely depends on iceberg productivity, fjord geometry, ocean currents, and the presence of sea ice.

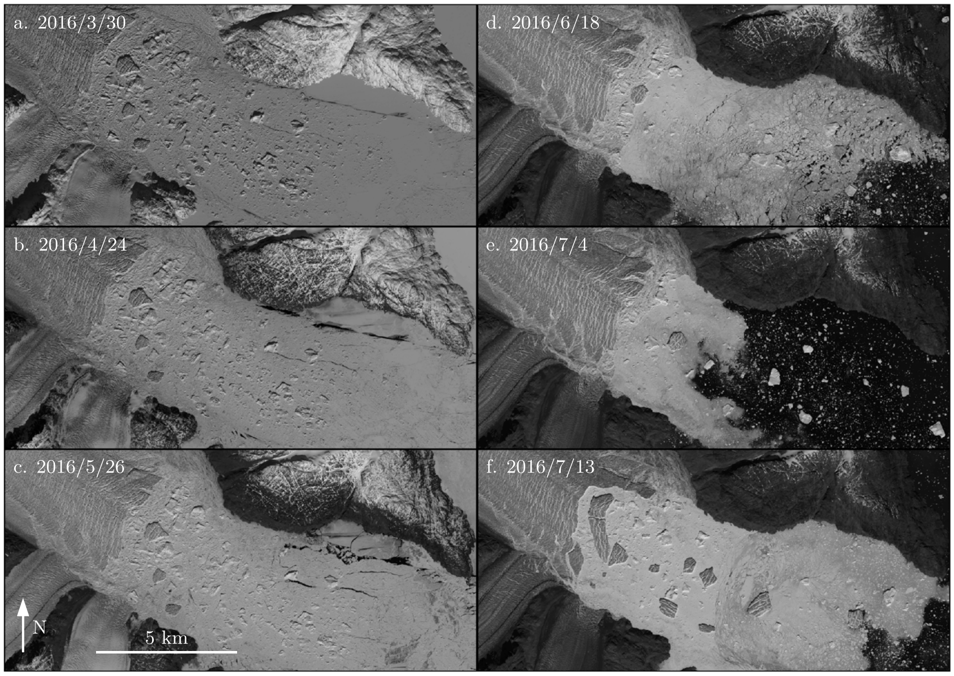

**Figure 1.** Landsat 8 images of Kangerdlugssuaq Glacier, Greenland, illustrating the breakup of ice mélange in the months leading up to the first major calving event of 2016.

In addition to potentially influencing iceberg calving and glacier dynamics, jamming of ice mélange controls the residence times of icebergs in fjords. Recent studies have indicated that iceberg melt is a major source of freshwater in fjords (Enderlin et al., 2016; Moon et al., 2017; Sulak et al., 2017) and therefore must influence fjord heat transport. Consequently, submarine melting of glacier termini, which in some cases represents a large fraction of the frontal ablation rate (Truffer & Motyka, 2016), is indirectly affected by the presence or absence of ice mélange and associated iceberg mobility.

A full assessment of the direct and indirect impacts of ice mélange on glacier dynamics requires knowledge of ice mélange rheology, which is currently lacking. Ice mélange clearly shares some similarities with sea ice, whose rheology has been studied extensively over the past several decades (Feltham, 2008). Continuum sea ice models typically invoke a viscoplastic rheology, but the exact form of the rheology is still an active area of research. Although knowledge of sea ice rheology can guide studies of ice mélange, it is important to note that ice mélange differs from sea ice in several distinct ways: (i) its thickness is highly heterogeneous and locally can be 10's to 100's of meters thick; (ii) icebergs are not planar, suggesting that ridging and rafting cannot produce as much horizontal strain in ice mélange as in sea ice; and (iii) flow is commonly driven from behind by an advancing glacier terminus, though stress from wind and ocean currents may also affect ice mélange motion and formation (e.g., Christoffersen et al., 2012). These differences in geometry and boundary conditions motivate observational and modeling studies that are tailored to understanding the behavior of ice mélange.

Published observations of ice mélange motion, which can be used to validate or negate potential constitutive relations, are limited to GPS surveys of individual icebergs (Amundson et al., 2010; Sutherland et al., 2014), short terrestrial radar surveys (Burton et al., 2018; Peters et al., 2015; Xie et al., 2018), and a handful of satellite-derived velocity fields (Foga et al., 2014; Joughin et al., 2008). Here we apply particle image velocimetry (PIV) to Landsat 8 imagery to produce ice mélange velocity fields at Greenland's three most productive glaciers (e.g., Rignot & Kanagaratnam, 2006): Jakobshavn Isbræ, Helheim Glacier, and Kangerdlugssuaq Glacier. These glacier-fjord systems were chosen for analysis because of their relative importance for the mass balance of the Greenland Ice Sheet and the persistent presence of ice mélange throughout the summer, which facilitates the generation of a greater number and variety of velocity fields. We then compare transverse profiles from the velocity fields to theoretical profiles derived from continuum descriptions of granular flow (Henann & Kamrin, 2013; Jop et al., 2006) and discuss potential resistive stresses from ice mélange and modeling of ice mélange dynamics. We choose to focus our analysis on continuum modeling, which is much more computationally efficient than discrete element models, with the goal of developing a modeling framework that is suitable for long-time scale (years to centuries) simulations of glaciers and ice sheets.

## 2. Methods

We derived velocity fields of ice mélange at Jakobshavn Isbræ, Helheim Glacier, and Kangerdlugssuaq Glacier using all available Landsat 8 Operational Land Imager scenes from 2013 to 2017; Landsat 8 has been operational since February 2013. We use the band 8 scenes, which are panchromatic and have a pixel size of 15 m. After removing all cloudy scenes, the remaining scenes were cropped to our regions of interest.

The image processing chain is similar to that of Fahnestock et al. (2016), with some modifications in order to better resolve velocity fields of relatively small regions. The images are first filtered using a Gaussian highpass filter with a three-pixel (45 m) standard deviation. The filter enhances edges of icebergs and helps to eliminate temporal changes in scene texture due to changes in illumination and shadows. Sequential images are then processed using normalized cross correlation, as implemented in the Python openPIV module (Taylor et al., 2010). We use a correlation window size of 64 by 64 pix (960 by 960 m) with 87.5% overlap (in other words, the distance between the centers of adjacent correlation windows is 8 pix, or 120 m). All correlations with a signal-to-noise ratio less than 1.5 are excluded. The resultant velocity fields are then smoothed with a 3 by 3 pix (45 by 45 m) median filter that ignores data gaps. Each velocity field is the result of processing temporally adjacent images (i.e., we did not apply any temporal averaging). We performed tests on the Landsat images and on synthetic images and found that decreasing the correlation window size resulted in noisier velocity fields but did not affect their overall structure.

Due to overlapping image scenes at high latitudes, it is possible to generate velocity fields that span time intervals that are shorter than Landsat 8's nominal repeat period of 16 days by using scenes from different path/row combinations. For certain applications, use of different path/row combinations would potentially introduce considerable error into the calculations due to orthorectification offsets. However, in our application the icebergs are located roughly along a horizontal plane and flow in the plane, and so the digital elevation model used to orthorectify the imagery should be highly accurate. In addition, (i) we are mostly interested in general spatial patterns, and (ii) icebergs tend to move relatively fast (>30 m/day) so that the signal-to-noise ratio is large. For comparison, apparent ground motion in the velocity fields is less than 1 m/day. Use of overlapping scenes from different path/row combinations greatly increase the number of image pairs that we are able to analyze, which is important because the flow of ice mélange is often too fast to be observed during a 16-day period, especially in summer when calving events are common.

## 3. Results

We generated 27, 32, and 82 velocity fields for Jakobshavn Isbræ, Helheim Glacier, and Kangerdlugssuaq Glacier, respectively, which amounts to about 10–20 velocity fields per year. The time interval between image pairs ranged from 2 to 30 days. Some of the velocity fields are extensive and span the entire fjord in question, whereas others are spotty or only cover a few kilometers of the fjord. The ability to resolve the velocity depends on the amount of motion in the fjord, which is typically greater in summer than winter due to a higher frequency of calving events and greater mobility within the ice mélange.

We observed uniform, extensional, and compressional flow. Uniform flow was most commonly observed, and was almost always observed during winter and spring (Figures 2 and 3a–3c). With the exception of one winter velocity field that was produced from imagery recorded shortly after a calving event, the wintertime flow at Helheim Glacier was remarkably steady.

Summer velocity fields were considerably more variable (Figures 3d–3f and 4). Flow was generally extensional at Jakobshavn Isbræ, especially within a few kilometers of the terminus. Conversely, flow was rarely extensional at Helheim Glacier and was often compressional. The ice mélange at Kangerdlugssuaq Glacier exhibited uniform, extensional, and compressional flow during various time periods in summer.

We were unable to detect any distinct seasonal or other temporal patterns in transverse velocity profiles. However, it is clear from Figures 2d–2f and 5 that most of the flow is accommodated in shear bands along the fjord walls that are about 1 km wide.

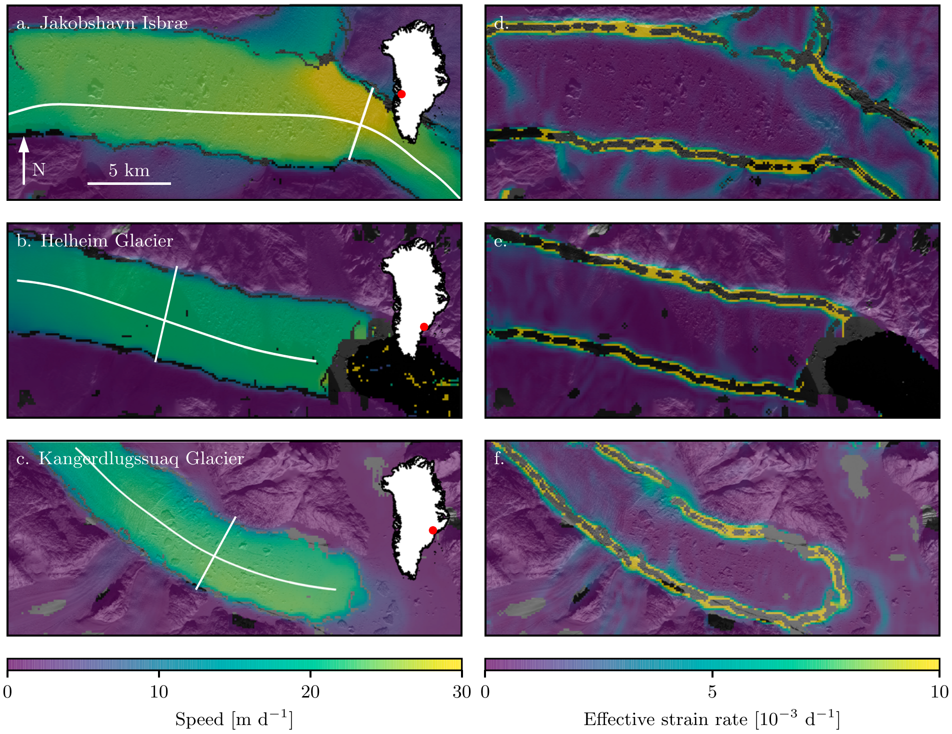

**Figure 2.** Typical winter velocity fields of ice mélange. (a)–(c) Speed and (d)–(f) effective strain rate at Jakobshavn Isbrae (top row; 17–24 February 2017), Helheim Glacier (middle row; 3–12 February 2014), and Kangerdlugssuaq Glacier (bottom row; 30 March to 6 April 2016). The orientation and scale are the same for all plots; locations within Greenland are shown in the insets. Gray regions indicate where image cross-correlation results were discarded due to low signal-to-noise ratios. The white curves indicate longitudinal streamlines and across-fjord transects used to plot velocity profiles in Figures 3 and 5. In (f), the band of high strain rates that extends across the fjord marks the end of cohesive ice mélange and indicates where ice mélange is pushing into sea ice.

## 4. Interpretation of Velocity Fields

The three flow regimes that we observe provide important insights into temporal and spatial variations in ice mélange rheology.

1. *Uniform flow* indicates that the ice mélange is tightly packed and that out-of-plane motion, such as iceberg rotation, ridging, and rafting, is not a dominant flow process. Ice mélange cohesiveness, as estimated by the ability of our PIV methods to resolve velocities far down fjord from the terminus, is often high during periods of steady flow. For example, during winter we are able to produce velocity fields at Jakobshavn Isbræ that extend 30 km down fjord, which is a distance of about six times the fjord width (Figure 3a). Although we occasionally generate similarly long velocity fields during summer, more commonly we are only able to resolve velocities within about 10 km of the terminus.
2. *Compressional flow* is typically only observed in velocity fields generated from image pairs that were closely spaced in time, and often appears to occur in the days following a calving event. Thus, compressional flow fields are observed almost exclusively in summer, when calving is most frequent (Figure 3). One exception is the lone outlier in the winter velocity profiles at Helheim Glacier (Figure 3b), which occurred after a large calving event displaced the ice mélange. GPS and time-lapse observations from Jakobshavn Isbræ indicate that during summer icebergs in the fjord experience an accordion-like motion, in which they are moving slower than the terminus following calving events, slowly accelerate over the course of several days until they are moving the same speed as the terminus, and eventually start to pull away from the terminus immediately prior to the next calving event (Amundson et al., 2010; Cassotto et al., 2015). Similarly, terrestrial radar data collected during calving events suggest that the packing fraction experiences a net reduction in response to calving events (Peters et al., 2015). These observations suggest that the density, or packing fraction, of the ice mélange evolves in response to calving events and that compressional flow occurs when

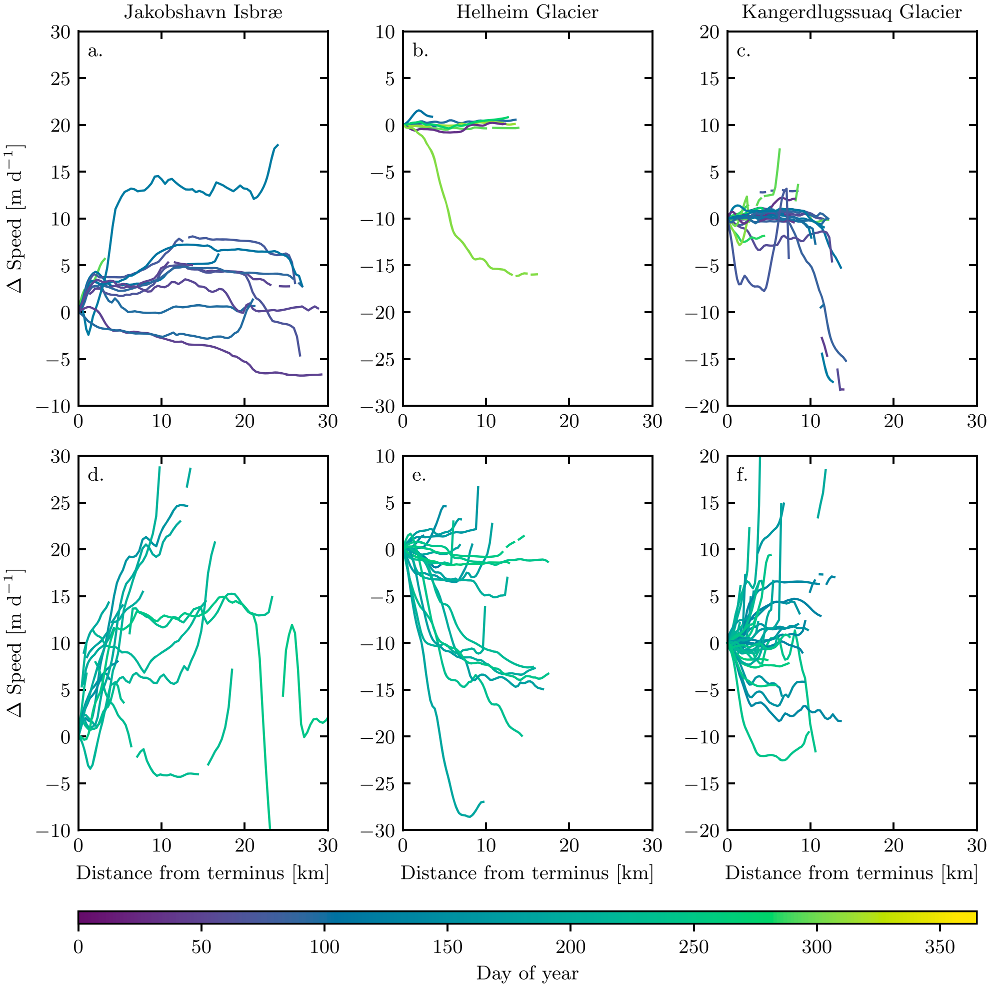

**Figure 3.** Longitudinal velocity profiles relative to terminus velocity for (a)–(c) winter and (d)–(f) summer. Summer is defined as consisting of May through September. Speeds are taken along the streamlines depicted in Figure 2.

the ice mélange is being recompacted. Compaction requires resistive stresses from the fjord walls, which likely increase as the icebergs become more highly packed and the ice mélange thickens.

3. *Extensional flow* is most commonly observed in summer and appears to be the dominant form of summertime flow at Jakobshavn Isbræ (Figure 3d; see also Burton et al., 2018). Extension occurs when ocean currents, wind, and/or buoyant torques on icebergs are able to overcome shear stresses in the ice mélange. Iceberg packing fraction likely decreases in the downfjord direction, resulting in enhanced iceberg mobility. The presence of extensional flow at Jakobshavn Isbræ points to the role of fjord geometry in affecting ice mélange mobility, as the fjord walls are diverging in the near-terminus region. This fjord geometry contrasts with Helheim Glacier, whose fjord is exceptionally straight and parallel-sided, and Kangerdlugssuaq Glacier, whose fjord is sinuous and has variable width.

In the following section, we use a continuum approach to analyze the quasi-static flow of ice mélange during winter and demonstrate that constitutive relations developed to describe granular flow in laboratory experiments do an adequate job of characterizing uniform flow of ice mélange. A major challenge, however, will be in modifying the constitutive relations to be able to account for the growth and decay of sea ice as well as variations in packing fraction and ice mélange composition that occur during periods of compressional and extensional flow.

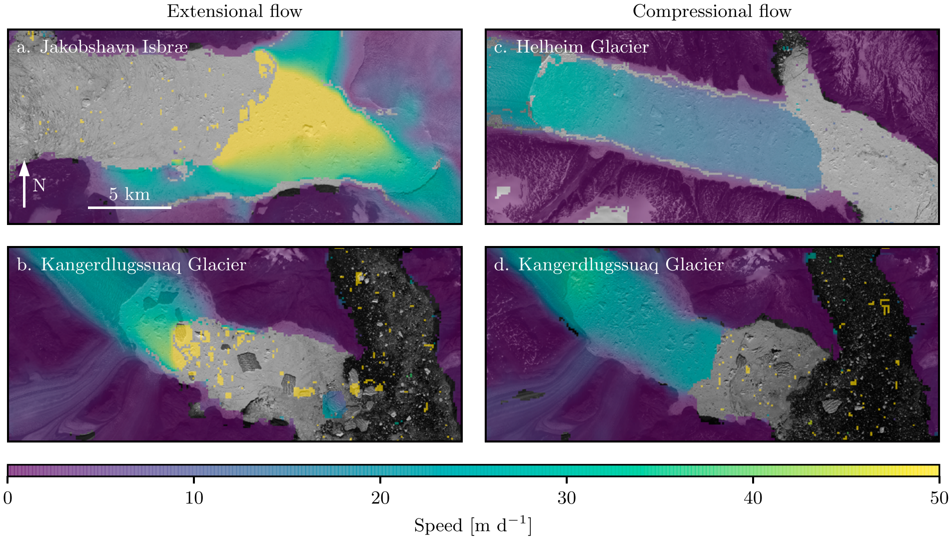

**Figure 4.** Example extensional (a)–(b) and compressional (c)–(d) flow regimes. Velocities were calculated over the following time intervals: (a) 8–10 June 2014, (b) 7–9 August 2014, (c) 16 July to 1 August 2015, and (d) 31 August to 2 September 2017. The orientation and scale are the same for all plots. Gray regions indicate where image cross-correlation results were discarded due to low signal-to-noise ratios.

## 5. Continuum Models of Ice Mélange

Ice mélange generally exhibits uniform flow in winter with only small variations in velocity in the along-fjord direction. This is especially true at Helheim Glacier, where the ice mélange flows through a straight fjord of uniform width. The winter flow regime is therefore analogous to a bulldozer slowly pushing a pile of gravel through a confined channel, with the exception that ice mélange is floating and has zero shear stress at its base (assuming negligible influence from drag or fjord currents). Thus, although out-of-plane motion is relatively unimportant under these conditions, shear stresses along the fjord walls should impose a thickness gradient on the ice mélange, as is observed in digital elevation models (Figure 6). We analyze flow under these quasi-static conditions to assess potential resistive stresses from ice mélange and to test the extent to which the flow can be approximated by continuum models of granular materials.

We begin by defining a number of variables that are required for describing the continuum models and for generating thickness and velocity profiles. These and all other variables are also listed in the Notation section. First, we define the strain rate tensor as $\dot{\epsilon}_{ij} = 1/2(\partial u_i/\partial x_j + \partial u_j/\partial x_i)$, where $u_i$ is the velocity component and $x_i$

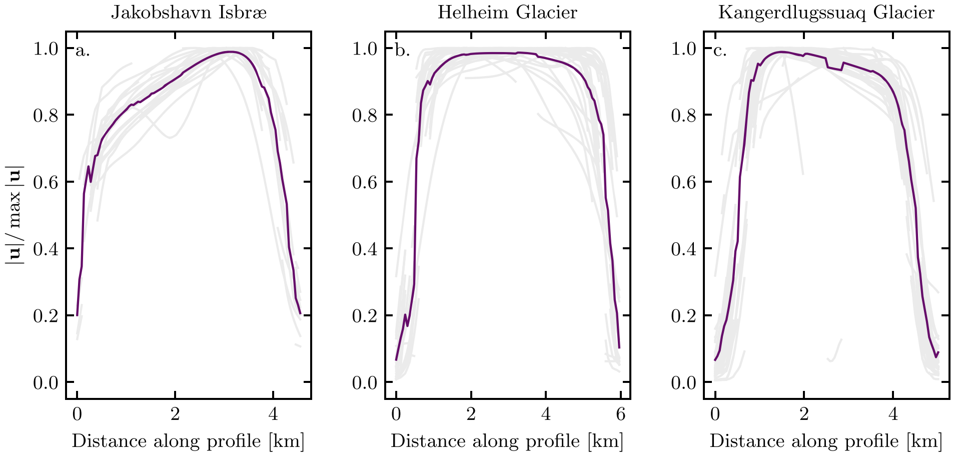

**Figure 5.** Normalized transverse velocity profiles for (a) Jakobshavn Isbræ, (b) Helheim Glacier, and (c) Kangerdlugssuaq Glacier. The dark profiles represent the mean of all profiles (gray). Speeds are taken along the transects indicated in Figure 2.

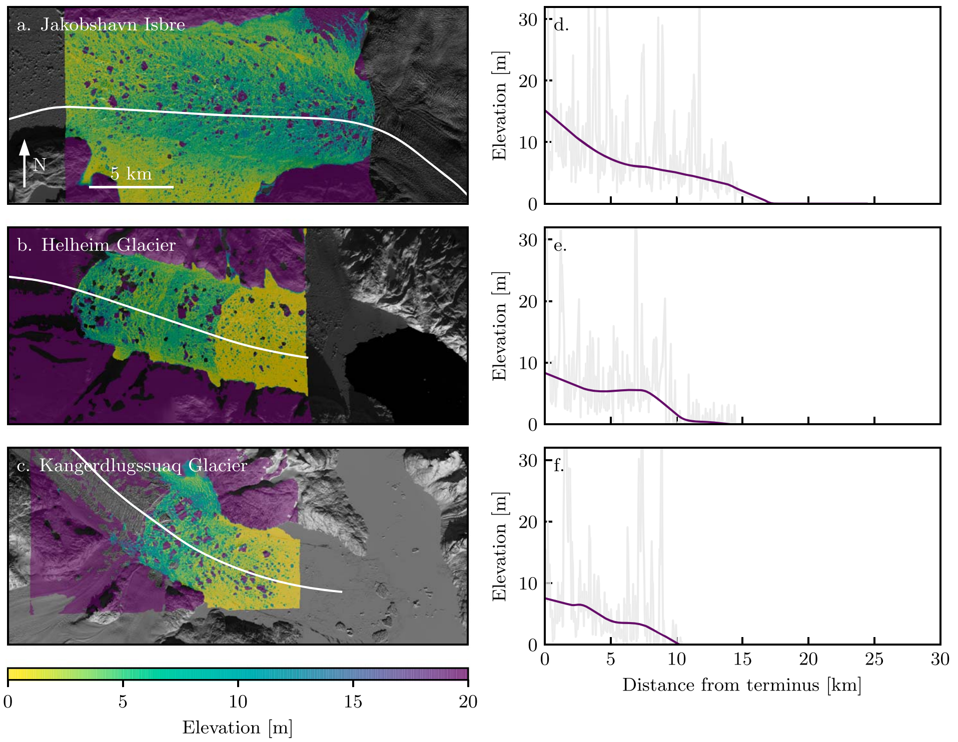

**Figure 6.** Digital elevation models of (a) Jakobshavn Isbræ (6 April 2011), (b) Helheim Glacier (16 October 2014), and (c) Kangerdlugssuaq Glacier (7 April 2016) from the ArcticDEM, after accounting for the local difference between the ellipsoid and the geoid. (d)–(f) Surface elevation profiles extracted along the streamlines shown in panels (a)–(c). Dark curves represent elevation profiles after application of a smoothing spline.

is the spatial coordinate. We use the Cauchy stress tensor $\sigma_{ij} = \sigma_{ji}$, which we partition into tectonic stresses $\sigma'_{ij}$ (referred to as *resistive stresses* in the glaciological literature; van der Veen, 2013) and the glaciostatic pressure $P$ by setting $\sigma_{ij} = \sigma'_{ij} - P\delta_{ij}$, where $\delta_{ij}$ is the Kronecker delta. The tectonic stress is related to the strain rate through a viscoplastic constitutive relationship, which we describe in section 5.1. We define the effective strain rate as $\dot{\epsilon}_e = (\dot{\epsilon}_{ij}\dot{\epsilon}_{ij}/2)^{1/2}$ and assume that the flow is incompressible, such that $\dot{\epsilon}_{kk} = 0$, as is commonly done for well-developed granular flows. Under steady flow conditions, the equations of motion are $\partial\sigma_{ij}/\partial x_j = \rho g \delta_{iz}$, where $\rho$ is the material density and $g$ is the acceleration due to gravity.

In addition, we make six simplifying approximations: (i) the fjord width is constant; (ii) the driving stress is entirely balanced by horizontal shear stresses, such that all strain rate components except $\dot{\epsilon}_{xy}$ can be neglected; (iii) the strain rates do not vary with depth; (iv) the pressure and ice mélange thickness are uniform across the width of the fjord; (v) ice mélange can be modeled using a single effective iceberg size; and (vi) the stress along the fjord walls is at the yield stress. We first use these assumptions to analyze the longitudinal thickness and pressure distributions, assess the coefficient of friction at the yield stress, and estimate the resistive force imposed on a glacier's terminus. We then use those results to constrain theoretical transverse velocity profiles, which we also compare to the satellite-derived velocities.

### 5.1. Thickness and Pressure Distributions

Under our approximations, vertical integration of the stress balance equations yields (e.g., van der Veen, 2013, pp. 48–50)

$$\frac{\mathrm{d}}{\mathrm{d}x}(H\sigma'_{xx}) + H\frac{\mathrm{d}\sigma'_{xy}}{\mathrm{d}y} = 2H\frac{\mathrm{d}\tilde{P}}{\mathrm{d}x}, \tag{2}$$

where all stresses are hereafter depth-averaged, $H$ is the ice mélange thickness, $\tilde{P}$ is the difference between the depth-averaged glaciostatic and hydrostatic pressures and is given by

$$\tilde{P} = \frac{1}{2}\rho g\left(1 - \frac{\rho}{\rho_w}\right)H, \tag{3}$$

and $\rho_w$ is the density of sea water. We assume a corresponding vertically integrated viscoplastic rheology in which

$$\sigma'_{ij} = \frac{\mu\tilde{P}}{\dot{\epsilon}_e}\dot{\epsilon}_{ij} + \tilde{P}_L\delta_{ij}, \tag{4}$$

where $\mu$ is an effective coefficient of friction and the subscript $L$ refers to properties evaluated at the end of the ice mélange (at $x = L$). In the granular rheologies that we consider in section 5.2, $\mu$ is a nonlinear function of $\dot{\epsilon}_e$ and may depend on the presence or absence of sea ice because, for example, sea ice may set a minimum yield stress that must be met even at low pressure. We do not explicitly account for sea ice in our analysis.

At the end of the ice mélange the depth-averaged stress must balance with the depth-averaged water pressure, such that

$$\sigma_{xx,L} = -\frac{1}{2}\rho g\frac{\rho}{\rho_w}H_L. \tag{5}$$

This same boundary condition applies to ice shelves and leads to extensional flow (van der Veen, 2013). However, the thickness of ice mélange approaches that of individual icebergs at $x = L$, and thus internal deformation should be minimal there. This is a well-known problem from sea ice modeling (Leppäranta, 2012) and is resolved by the inclusion of the $\tilde{P}_L\delta_{ij}$ term in equation (4), which forces the longitudinal strain rate to equal 0 at $x = L$ (e.g., Hibler, 2001).

Due to our assumption that $\dot{\epsilon}_{xy}$ is the only nonzero strain rate component, we can simplify the flow equations by noting that

$$\frac{\dot{\epsilon}_{ij}}{\dot{\epsilon}_e} = \operatorname{sgn}\left(\frac{W}{2} - y\right). \tag{6}$$

Consequently, all across-fjord variations in flow are determined by $\mu$ and the flow is symmetric around the fjord centerline. Inserting equations (4) and (6) into equation (2) and dividing by $\rho g(1 - \rho/\rho_w)/2$ yields

$$H_L\frac{\mathrm{d}H}{\mathrm{d}x} + H^2\frac{\mathrm{d}\mu}{\mathrm{d}y}\operatorname{sgn}\left(\frac{W}{2} - y\right) = 2H\frac{\mathrm{d}H}{\mathrm{d}x}. \tag{7}$$

Integrating equation (7) across the width of the fjord results in

$$H_L\frac{\mathrm{d}H}{\mathrm{d}x} - 2H^2\left(\frac{\mu_0}{W}\right) = 2H\frac{\mathrm{d}H}{\mathrm{d}x}, \tag{8}$$

where $\mu_0$ is the coefficient of friction at the yield stress and $W$ is the fjord width. The yield stress, $\mu_0\tilde{P}$, decreases in the flow direction (see also Burton et al., 2018); it equals 24.3 kPa for $\mu_0 = 0.5$ and $H = 100$ m and is about a factor of four smaller at $x = L$ (assuming that the effective iceberg size is 25 m). These values are lower than, but of the same order of magnitude as, the yield stress for ice shelves (van der Veen, 2013). The solution to equation (8) is given by the implicit exponential function

$$H = H_L \exp\left\{\mu_0\frac{(L - x)}{W} + \frac{H - H_L}{2H}\right\}. \tag{9}$$

Equation (9) can be solved numerically and combined with equation (3) to determine $\tilde{P}(x)$. In section 5.2 we will use $\tilde{P}(x)$, along with the constitutive equation (equation (4)), to investigate variations in transverse velocity profiles along the length of a fjord.

Finally, the width-averaged force exerted against a glacier's terminus (at $x = 0$) is given by $-\sigma_{xx,0}H_0$. This force includes the force due to water pressure, which would also act on a glacier in the absence of any ice mélange. We therefore calculate the *excess* force acting on a glacier's terminus by subtracting the depth-integrated water pressure. Recalling that $\sigma_{xx} = \sigma'_{xx} - P$, we arrive at

$$F/W = \frac{1}{2}\rho g\left(1 - \frac{\rho}{\rho_w}\right)\left(1 - \frac{H_L}{H_0}\right)H_0^2, \tag{10}$$

with $H_0$ determined by evaluating equation (9) at $x = 0$.

In Figure 7 we plot ice mélange profiles and the force per unit width acting on the glacier terminus for various combinations of $L/W$, and $\mu_0$. We find that values of $\mu_0$ ranging from about 0.3 to 0.5 are required to produce thickness profiles that roughly agree with observations (compare Figures 6 and 7). However, changing

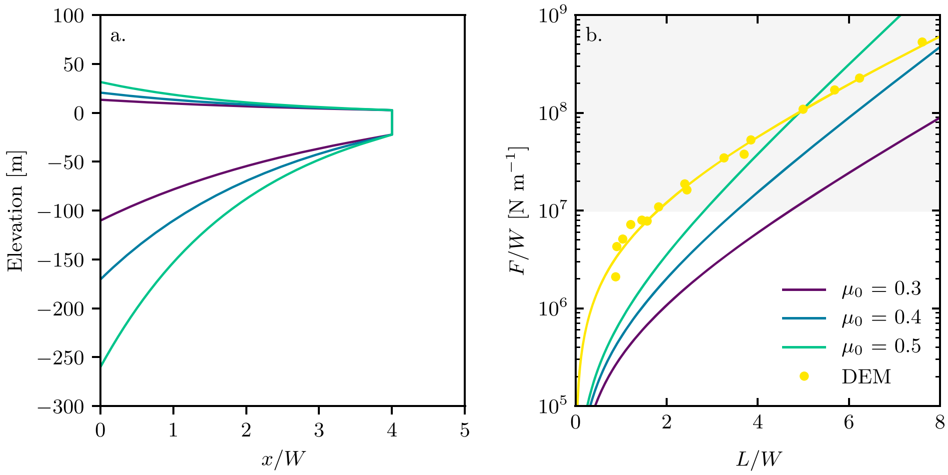

**Figure 7.** Theoretical ice mélange geometries and width-averaged forces acting on glacier termini for $H_L$ = 25 m and $W$ = 5,000 m. (a) Steady-state ice mélange profiles for various values of $\mu_0$. (b) Width-averaged force acting on glacier termini versus the ice mélange length-to-width ratio. Yellow dots indicate values derived from two-dimensional discrete element simulations (Burton et al., 2018) and the yellow curve is the result from the continuum model using $H_L$ = 100 m and $\mu_0$ = 0.25. The gray shaded region indicates the force per unit width that is required to prevent the bottom-out capsize of 1,000-m tall icebergs, such as are commonly observed to calve from large outlet glaciers in Greenland. This calculation assumes that the force is exerted along a horizontal line at sea level and that ice mélange does not exert a vertical force on an iceberg as it capsizes (Amundson et al., 2010). Since ice mélange has a finite thickness of 100–200 m and most of the ice is below sea level, the actual force needed to inhibit iceberg capsize may be about a factor of two smaller than estimated. DEM = discrete element model.

$\mu_0$ has a relatively minor impact on the surface elevation due to the fact that ice mélange is floating. The flotation condition, coupled with the highly heterogeneous nature of ice mélange, makes it difficult to pin down an appropriate value of $\mu_0$ based solely on the thickness profile, which in addition is affected by surface and submarine melting. Nonetheless, our values for the coefficient of friction at the yield stress are within the range of reported friction coefficients of ice rubble and sea ice, which range from about 0.1 to greater than 1 but most commonly fall between 0.3 and 0.5 (e.g., Ettema & Urroz, 1989; Liferov & Bonnemaire, 2005; Lishman et al., 2011; Sukhorukov & Løset, 2013, Tuhkuri & Lensu, 1997). We find that the load required to inhibit calving of 1,000-m thick icebergs is reached when $L/W \sim 3$. The force curves follow a similar trajectory to results from discrete element modeling but result in lower magnitudes. Moreover, the force curves from the continuum model can be made to match the results from the discrete element model by setting $H_L = 100$ m and $\mu_0 = 0.25$, effectively making the ice mélange thicker and flatter. The good agreement between the discrete element simulations and the continuum model occurs because both predict an exponential relationship between $F/W$ and $L/W$ (Burton et al., 2018; see also section 5.3).

### 5.2. Transverse Velocity Profiles

Here we generate theoretical velocity profiles for two constitutive relations for granular flow: the $\mu(I)$ rheology (Jop et al., 2006) and the *nonlocal* granular fluidity rheology (Henann & Kamrin, 2013) in which the viscosity depends on distant stresses. These constitutive relations are appealing because they are less computationally expensive than other recent attempts to model the flow of ice mélange as they do not require tracking of individual icebergs (Burton et al., 2018; Robel, 2017; Vaňková & Holland, 2017). We are additionally motivated to test whether these rheologies, which have been developed from laboratory scale experiments, scale up to geophysical settings.

In the following analysis, we restrict ourselves to the half-space $y \in [0, W/2]$, so that the strain rate $\dot{\epsilon}_{xy}$ is always positive. In both the $\mu(I)$ and nonlocal rheologies, the strain rate is nonlinearly related to the coefficient of friction $\mu$, which varies across the fjord. A simple relationship for $\mu$ can be found by subtracting equation (8) from equation (7) and integrating the result from $y = 0$ to $y$, which yields

$$\mu = \mu_0 \left(1 - \frac{2y}{W}\right). \tag{11}$$

Deriving velocity profiles involves relating equation (11) to the strain rate and integrating. During the integration we require that the mean velocity across the profile equal the terminus velocity in order to satisfy the conditions of quasi-static flow; thus, the velocity at $y = 0$, $W$ is not equal to zero and is instead determined as part of the integration procedure.

### 5.2.1. $\mu(I)$ Rheology

In the $\mu(I)$ rheology, the coefficient of friction is a function of the inertial number $I$ and is expressed as

$$\mu = \mu_s + \frac{I(\mu_0 - \mu_s)}{I_0 + I}, \tag{12}$$

where $\mu_s$ is the minimum coefficient of friction and $I_0$ is a constant. The coefficient of friction only approaches $\mu_0$, and therefore when evaluating equation (11) we must subtract some small value to ensure that the friction coefficient on the fjord walls is slightly smaller than $\mu_0$. The inertial number is the ratio of inertial forces to imposed forces acting on grains and is given by

$$I = \frac{\dot{\epsilon}_e d}{\sqrt{\tilde{P}/\rho}}, \tag{13}$$

where $d$ is the grain size and $\rho$ is the density. Thus, the effective friction coefficient has a value of $\mu_s$ when the strain rate equals zero and goes toward a limiting value of $\mu_0$ for high strain rates and low pressures. The value of $I$ indicates whether the flow is quasi-static ($I < 10^{-3}$), dense ($10^{-3} < I < 10^{-1}$), or collisional ($I > 10^{-1}$). Using an effective strain rate of $\dot{\epsilon}_e = 10^{-3}\text{d}^{-1}$ (Figure 2), and a typical iceberg size of $d = 25$ m, we find that the inertial number for ice mélange is $\sim 10^{-7}$ during periods of steady flow, which is well within the quasi-static range.

Inserting equation (13) into equation (12), noting that $\dot{\epsilon}_e = (\text{d}u/\text{d}y)/2$, and rearranging, we find that

$$\frac{\text{d}u}{\text{d}y} = -2\frac{I_0}{d}\sqrt{\frac{\tilde{P}}{\rho}}\left(\frac{\mu - \mu_s}{\mu - \mu_0}\right). \tag{14}$$

The pressure in equation (14) is given by equation (3). Although equation (14) can be solved analytically (see Tankeo et al., 2013), we choose to solve it numerically for brevity and to make a more natural comparison to the nonlocal rheology, which we are unable to solve analytically.

Equation (14) is only valid where the shear stress is high enough to cause deformation of the material. The region in which deformation occurs can be determined by noting that $\mu_s \leq \mu \leq \mu_0$. We have already assumed that the margins are at the yield stress, and therefore we only need to address the left hand side of the inequality. Thus, according to equation (11), the critical value $y_c$ beyond which deformation no longer occurs is given by

$$y_c = \frac{W}{2}\left(1 - \frac{\mu_s}{\mu_0}\right). \tag{15}$$

We evaluate equation (11) and then integrate equation (14) from $y = 0$ to $y = y_c$ using a centered difference approximation and boundary conditions of $u(0) = u_0$ and $\text{d}u/\text{d}y = 0$ at $y = y_c$. The velocity is held constant from $y = y_c$ to $y = W/2$. After solving for $u(y)$, the velocity $u_0$ is adjusted until the mean velocity across the profile equals the glacier terminus velocity, defined as equaling 50 m/day.

Velocity profiles generated using the $\mu(I)$ rheology depend on the coefficients of friction, the effective pressure, the grain size, the constant $I_0$, and the ice mélange length, width, and thickness $H_L$. Although the width of the shear zone does not vary with length, the amount of deformation that occurs within the shear zone decreases in the flow direction due to the reduction in the effective pressure (Figure 8a). Consequently, the flow becomes increasing plug like and the sliding velocity along the fjord walls increases. Variations in grain size and $I_0$ have opposite effects. Decreasing the grain size or increasing $I_0$ results in faster flow, which means that the sliding velocity does not need to be as large to maintain a constant mean velocity across the profiles (Figures 8b–8c). We will address the effect of changing $\mu_s$ below.

### 5.2.2. Nonlocal Rheology

The nonlocal rheology attempts to account for the effect of force chains on quasi-static flow by relating the effective friction coefficient to distant stresses through a parameter referred to as the granular fluidity. In the nonlocal rheology, the effective friction coefficient is given by

$$\mu = \frac{\dot{\epsilon}_e}{g'}, \tag{16}$$

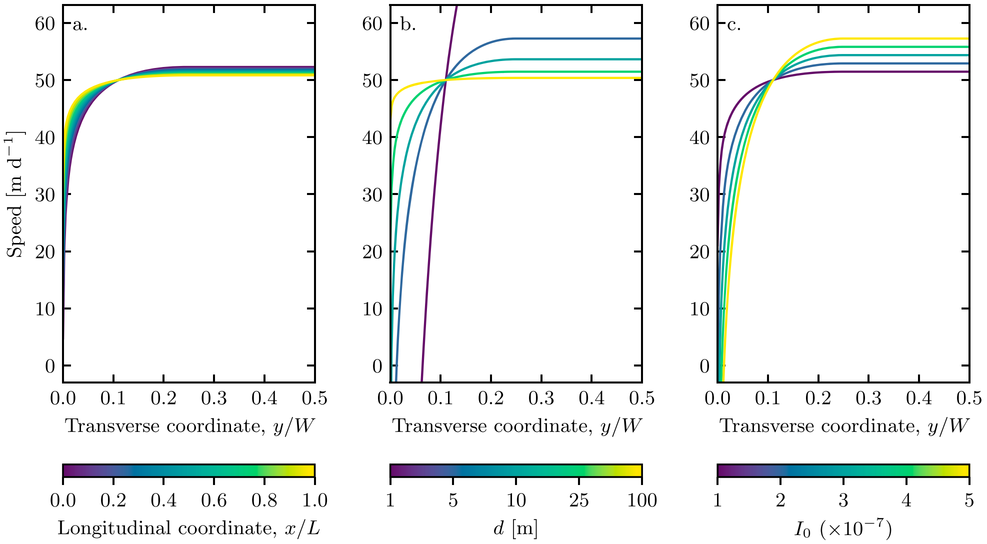

**Figure 8.** Effect of model parameters on theoretical profiles predicted by the $\mu(I)$ rheology. For all profiles $\mu_0 = 0.4$, $\mu_s = 0.2$, $W = 5$ km, and $L = 20$ km. (a) Variations in profiles along the length of the fjord for $d = H_L = 25$ m, $I_0 = 10^{-7}$, and $\tilde{P}$ prescribed by equation (3). (b) Profiles at $x/L = 0.5$ for various $d$. (c) Profiles at $x/L = 0.5$ for various $I_0$. The negative values found in (b) and (c) occur because we have required the mean velocity to be the same across all profiles.

where $g'$ is the granular fluidity. The granular fluidity depends on both local and distant stresses through the differential relation

$$\nabla^2 g' = \frac{1}{\xi^2}(g' - g'_{\text{loc}}), \tag{17}$$

where $g'_{\text{loc}}$ is the local granular fluidity and $\xi$ is the cooperativity length that dictates the distances over which stresses are transferred through the material. Following experiments that suggest a Bingham-like form for $\mu$, $g'_{\text{loc}}$ is defined as

$$g'_{\text{loc}} = \begin{cases} \sqrt{\frac{\tilde{P}}{\rho d^2}} \frac{(\mu - \mu_s)}{\mu b} & \text{if} \mu > \mu_s, \\ 0, & \text{if } \mu \leq \mu_s \end{cases} \tag{18}$$

for dimensionless constant $b$. Finally, the cooperativity length, which describes the distance over which stresses influence flow of distant grains, is given as

$$\xi = \frac{Ad}{\sqrt{|\mu - \mu_s|}}, \tag{19}$$

where $A$ is a dimensionless constant that characterizes the amplitude of the cooperativity.

Using the same assumptions as previously and rearranging equation (16), we find that

$$\frac{\mathrm{d}u}{\mathrm{d}y} = 2\mu g'. \tag{20}$$

We solve for the granular fluidity, which depends on $\mu$, by numerically integrating equation (17) using standard difference formulas with boundary conditions of $dg/dy = 0$ at $y = 0, W/2$ (as recommended by Henann & Kamrin, 2013) and noting that $\mu$ is given by equation (11). Equation (20) is then integrated to solve for $u$.

The velocity profiles predicted by the nonlocal rheology exhibit more along-fjord variability and tend to be less rounded than those predicted by the $\mu(I)$ rheology, but have a similar grain size dependency (Figures 9a–9b). Increasing the dimensionless parameter $A$ makes the profiles more rounded, but also causes deformation to occur farther into the interior of the ice mélange because stress coupling allows deformation to occur at low shear stresses.

In Figure 10 we compare normalized velocity profiles from Helheim Glacier to theoretical profiles from both rheologies for various values of $\mu_s$. The effect of changing $\mu_s$, while holding $\mu_0$ fixed, is to change the width of the shear zone. In the $\mu(I)$ rheology the width of the shear zone is fixed by $y_c$ (given in equation (15), whereas in the nonlocal rheology deformation can occur beyond $y_c$. Consequently, the best agreement between observations and theory occurs at lower values of $\mu_s$ in the $\mu(I)$ rheology than in the nonlocal rheology.

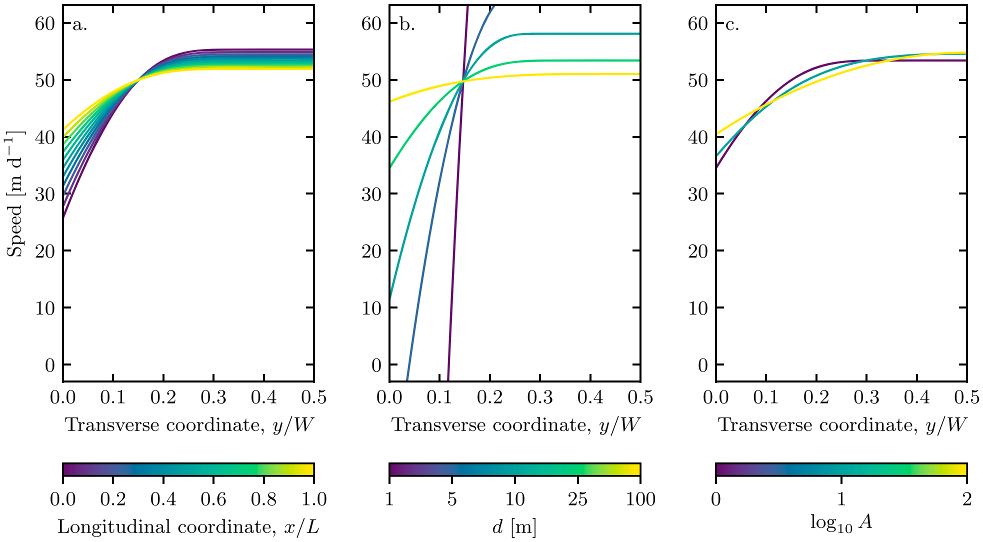

**Figure 9.** Effect of model parameters on theoretical profiles predicted by the nonlocal rheology. For all profiles $\mu_0 = 0.4$, $\mu_s = 0.2$, $W = 5$ km, and $L = 20$ km. (a) Variations in profiles along the length of the fjord for $d = H_L = 25$ m, $A = 1$, $b = 2 \times 10^5$, and $\tilde{P}$ prescribed by equation (3). (b) Profiles at $x/L = 0.5$ for various $d$. (c) Profiles at $x/L = 0.5$ for various $A$. Effect of $b$ on the profiles is not shown, but has an effect opposite to the grain size in that larger values of $b$ increase the flow speeds. The negative values found in (b) occur because we have required the mean velocity to be the same across all profiles.

### 5.3. Two-Dimensional Discrete Element Models

The continuum rheology (equation (4)) leads to an exponential thickness/pressure distribution along the length of the ice mélange (equation (9)). This agrees well with the exponential distribution shown in Burton et al. (2018), where a purely two-dimensional discrete element model was used to model ice mélange. A similar two-dimensional model was used in another recent study by Robel (2017). However, the depth-integrated continuum equations represent a fundamentally different response to increased pressure. As the terminus pushes the ice mélange, the increase in stress mostly causes the icebergs to either rotate or buckle into and out of the water (suggesting that some ridging and rafting may occur, although likely not to the same extent as in sea ice). The work done by the increase in pressure is thus stored as gravitational potential energy. In two-dimensional discrete element models, the work done is stored as compression of the individual grains, leading to an increase in the density of the system.

Nevertheless, an exponential pressure distribution is a natural feature of jammed, granular, discrete element models. In two-dimensional models where the particles feel a repulsive force upon geometric overlap, the

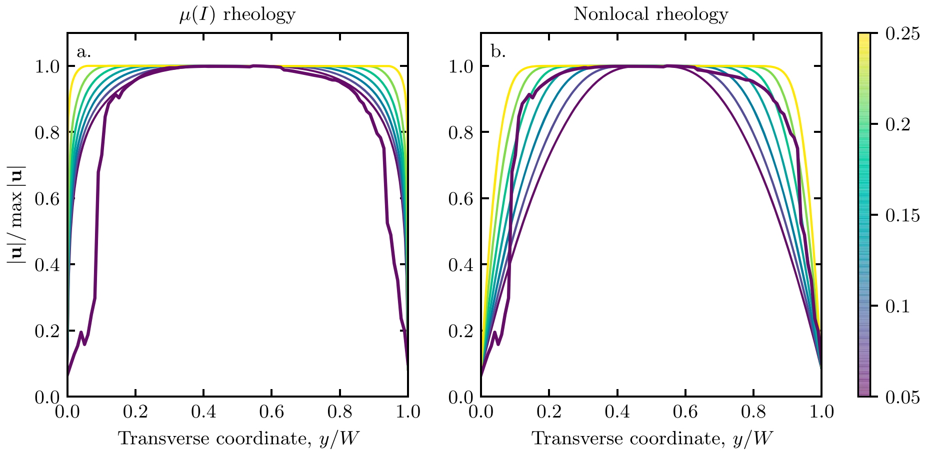

**Figure 10.** Comparison of transverse velocity profiles from Helheim Glacier (bold lines) to theoretical profiles for the (a) $\mu(I)$ and (b) nonlocal rheologies for $\mu_0 = 0.4$ and various values of $\mu_s$.

pressure in the system scales as $P_d \propto (\phi - \phi_c)^\alpha$, where $\phi$ is the two-dimensional area fraction of the system (density) and $\phi_c$ is the critical density at which the system jams, that is, particles begin to overlap (O'Hern et al., 2003). The exponent $\alpha$ characterizes the dependence of the repulsive force on the degree of particle overlap. For example, for harmonic, spring-like interactions between particles, $\alpha = 1$. In these systems, upon the application of shear, the yield stress has been shown to scale as $\sigma_0 \propto (\phi - \phi_c)^\gamma$, where $\gamma \approx \alpha$ with small corrections (Bonn et al., 2017; Olsson & Teitel, 2012). After integrating equation (2) across the width of the fjord (and replacing the driving stress $\tilde{P}/2$ with $P_d$), one arrives at

$$\frac{\mathrm{d}P_d}{\mathrm{d}x} \propto \sigma_0 \propto P_d, \tag{21}$$

leading to an exponential pressure distribution along the length of the fjord. Thus, although the fundamental mechanism of deformation in the granular material is different in real ice mélange, the two-dimensional discrete element models seem to capture the salient features of granular flow of ice mélange despite not accounting for out-of-plane motion.

## 6. Conclusions

Ice mélange velocity fields vary seasonally. The velocity fields are typically uniform and steady in winter, whereas they tend to be more highly variable in summer and can be steady, extensional, or compressional. At all times, though, ice mélange exhibits signs of viscoplastic deformation, with concentrated regions of deformation near fjord walls and plug-like flow in the interior. The shear zones typically span 10–20% of the fjord widths.

Comparison of transverse velocity and longitudinal thickness profiles with theoretical profiles derived from constitutive relations for granular flow, under the conditions of quasi-static granular flow, shows good agreement and provide an avenue for future development of ice mélange flow models. In particular we analyzed two granular rheologies: the $\mu(I)$ rheology (Jop et al., 2006) and the nonlocal rheology (Henann & Kamrin, 2013). The shape of the velocity profiles predicted by both rheologies depends on the pressure (and therefore ice mélange thickness), the coefficients of friction at the yield stress $\mu_0$ and at low strain rates $\mu_s$, and the characteristic iceberg size $d$. We find that $\mu_0 \approx 0.4$ yields thickness profiles that are consistent with observations. Larger values of $\mu_0$ result in thicker ice mélange and larger longitudinal thickness gradients; because the velocity profiles depend on pressure, higher values of $\mu_0$ also cause greater variations in the velocity profiles along the length of the fjord. Assuming a value of $\mu_0 = 0.4$, we find good agreement between theoretical velocity profiles and observations in the $\mu(I)$ and nonlocal rheologies when $\mu_s$ is about 0.05 and 0.2, respectively. For both rheologies, we find that the characteristic iceberg size should be roughly 25 m, with larger values resulting in more plug-like flow.

Many challenges remain for ice mélange flow modeling. In particular, our comparison with constitutive relations for granular flow did not directly account for binding effects from sea ice and assumed incompressibility, uniform ice mélange thickness and iceberg dimensions, steady flow through a straight channel, and stresses being at the yield stress along the fjord walls. These assumptions may be adequate for characterizing quasi-static flow conditions, but are unable to account for the compressional and extensional flow regimes that are often observed in summer. Moreover, the friction coefficients are likely to vary seasonally through a dependence on interstitial sea ice, and ocean currents and wind are likely to exert nonnegligible stresses on ice mélange that may tend to pull it apart. Although our analysis provides some support for the use of idealized continuum rheologies of ice mélange, future work should attempt to account for heterogeneous iceberg size distributions, test granular rheologies under a wider variety of conditions, and compare model results to observed thickness and velocity profiles. Our results underscore the need to better resolve ice mélange characteristics in the field, which is clearly a challenging endeavor.

The continuum approach that we have adopted here, in lieu of discrete element modeling, will facilitate development of coupled glacier-ice mélange models. For situations in which simplified approximations of ice mélange stresses are preferred, such as in long-time scale ice sheet modeling, both continuum and discrete element models suggest that the width-averaged force that ice mélange exerts on glacier termini increases exponentially with the ice mélange length-to-width ratio and becomes sufficiently large to inhibit iceberg calving when the ratio exceeds about 3. It is encouraging that preliminary results from continuum and discrete element models are in agreement with each other.

## Notation

$L_g$ Glacier length
$U_t$ Terminus velocity
$U_f$ Frontal ablation rate; sum of iceberg calving rate and submarine melting
$u_i$ Velocity vector
$x_i$ Spatial coordinate
$x$ Along-fjord coordinate
$y$ Transverse coordinate
$y_c$ Critical value of $y$ beyond which no deformation occurs in the $\mu(I)$ rheology and at which there is a transition in $g'_{loc}$ in the nonlocal rheology
$W$ Ice mélange width
$L$ Ice mélange length
$H$ Ice mélange thickness
$g$ Gravitational acceleration
$\rho$ Ice density
$\rho_w$ Seawater density
$\dot{\epsilon}_{ij}$ Strain rate tensor
$\dot{\epsilon}_e$ Effective strain rate or the second invariant of the strain rate tensor
$\sigma_{ij}$ Cauchy stress tensor
$\sigma'_{ij}$ Tectonic stress tensor
$P$ Glaciostatic pressure
$\tilde{P}$ Effective pressure, taken to be the difference between glaciostatic pressure and hydrostatic pressure from seawater
$P_d$ Pressure in two-dimensional discrete element models of ice mélange
$\delta_{ij}$ Kronecker delta
$\mu$ Effective friction coefficient
$\mu_s$ Friction coefficient at low strain rates
$\mu_0$ Friction coefficient at the yield stress
$I$ Inertial number, which is the ratio of inertial forces to imposed forces acting on grains
$I_0$ Material constant that controls variations in the effective friction coefficient in the $\mu(I)$ rheology
$d$ Grain size
$g'$ Granular fluidity
$g'_{loc}$ Local granular fluidity
$\xi$ Cooperativity length
$b$ Dimensionless constant in the nonlocal rheology that affects the local granular fluidity
$A$ Dimensionless constant in the nonlocal rheology that affects the cooperativity length
$\phi$ Two-dimensional area fraction (density)
$\phi_c$ Critical value of $\phi$ at which a system jams
$\alpha$ Exponent that characterizes the dependency of the pressure on the proximity to the jamming point
$\gamma$ Exponent that characterizes the dependency of the yield stress on the proximity to the jamming point

**Acknowledgments**
Funding for this project was provided by the U.S. National Science Foundation (DMR-1506446 and DMR-1506307). Landsat 8 data used in this study are freely available from the USGS through https://glovis.usgs.gov/. Digital elevation models were provided by the Polar Geospatial Center under the U.S. National Science Foundation (OPP-1043681, OPP-1559691, and OPP-1542736) and are available from https://www.pgc.umn.edu/data/arcticdem/. Python code used to produce theoretical thickness and velocity profiles is provided as Supplementary Information.

## References

Amundson, J. M., Fahnestock, M., Truffer, M., Brown, J., Lüthi, M. P., & Motyka, R. J. (2010). Ice mélange dynamics and implications for terminus stability, Jakobshavn Isbræ, Greenland. *Journal of Geophysical Research*, *115*, F01005. https://doi.org/10.1029/2009JF001405

Amundson, J. M., & Truffer, M. (2010). A unifying framework for iceberg-calving models. *Journal of Glaciology*, *56*(199), 822–830. https://doi.org/10.3189/002214310794457173

Bonn, D., Denn, M. M., Berthier, L., Divoux, T., & Manneville, S. (2017). Yield stress materials in soft condensed matter. *Reviews of Modern Physics*, *89*, 35005. https://doi.org/10.1103/RevModPhys.89.035005

Burton, J. C., Amundson, J. M., Cassotto, R., Kuo, C.-C., & Dennin, M. (2018). Quantifying flow and stress in ice mélange, the world's largest granular material. *Proceedings of the National Academy of Sciences*, *115*, 5105–5110. https://doi.org/10.1073/pnas.1715136115

Cassotto, R., Fahnestock, M., Amundson, J. M., Truffer, M., & Joughin, I. (2015). Seasonal and interannual variations in ice mélange and its impact on terminus stability, Jakobshavn Isbræ, Greenland. *Journal of Glaciology*, *61*, 76–88. https://doi.org/10.3189/2015JoG13J235

Christoffersen, P., O'Leary, M., van Angelen, J. H., & van den Broeke, M. (2012). Partitioning effects from ocean and atmosphere on the calving stability of Kangerdlugssuaq Glacier, East Greenland. *Annals of Glaciology*, *53*, 249–256. https://doi.org/10.3189/2012AoG60A087

Enderlin, E. M., Hamilton, G. S., Straneo, F., & Sutherland, D. A. (2016). Iceberg meltwater fluxes dominate the freshwater budget in Greenland's iceberg-congested glacial fjords. *Geophysical Research Letters*, *43*, 11,287–11,294. https://doi.org/10.1002/2016GL070718

Ettema, R., & Urroz, G. E. (1989). On internal friction and cohesion in unconsolidated ice rubble. *Cold Regions Science and Technology*, *16*, 237–247. https://doi.org/10.1016/0165-232X(89)90025-6

Fahnestock, M., Scambos, T., Moon, T., Gardner, A., Haran, T., & Klinger, M. (2016). Rapid large-area mapping of ice flow using Landsat 8. *Remote Sensing of Environment*, *185*, 84–94. https://doi.org/10.1016/j.rse.2015.11.023

Feltham, D. L. (2008). Sea ice rheology. *Annual Review of Fluid Mechanics*, *40*, 91–112. https://doi.org/10.1146/annurev.fluid.40.111406.102151

Foga, S., Stearns, L. A., & van der Veen, C. J. (2014). Application of satellite remote sensing techniques to quantify terminus and ice mélange behavior at Helheim Glacier, East Greenland. *Marine Technology Society Journal*, *48*, 81–91. https://doi.org/10.4031/MTSJ.48.5.3

Fried, M. J., Catania, G. A., Stearns, L. A., Sutherland, D. A., Bartholomaus, T. C., Shroyer, E., & Nash, J. (2018). Reconciling drivers of seasonal terminus advance and retreat at 13 Central West Greenland tidewater glaciers. *Journal of Geophysical Research: Earth Surface*, *123*, 1590–1607. https://doi.org/10.1029/2018JF004628

Henann, D. L., & Kamrin, K. (2013). A predictive, size-dependent continuum model for dense granular flows. *Proceedings of the National Academy of Sciences*, *110*(17), 6730–6735. https://doi.org/10.1073/pnas.1219153110

Hibler, W. D. (2001). Sea ice fracturing on the large scale. *Engineering Fracture Mechanics*, *68*(17), 2013–2043. https://doi.org/10.1016/S0013-7944(01)00035-2

Howat, I. M., Box, J. E., Ahn, Y., Herrington, A., & McFadden, E. M. (2010). Seasonal variability in the dynamics of marine-terminating outlet glaciers in Greenland. *Journal of Glaciology*, *56*, 601–613. https://doi.org/10.3189/002214310793146232

Jop, P., Forterre, Y., & Poulique, O. (2006). A constitutive law for dense granular flows. *Nature*, *441*, 727–730. https://doi.org/10.1038/nature04801

Joughin, I., Howat, I. M., Fahnestock, M., Smith, B., Krabill, W., Alley, R. B., et al. (2008). Continued evolution of Jakobshavn Isbræ following its rapid speedup. *Journal of Geophysical Research*, *113*, F04006. https://doi.org/10.1029/2008JF001023

Joughin, I., Smith, B. E., Howat, I. M., Floricioiu, D., Alley, R. B., Truffer, M., & Fahnestock, M. (2012). Seasonal to decadal scale variations in the surface velocity of Jakobshavn Isbrae, Greenland: Observation and model-based analysis. *Journal of Geophysical Research*, *117*, F02030. https://doi.org/10.1029/2011JF002110

Leppäranta, M. (2012). *The drift of sea ice* (2nd ed.). Berlin and Heidelberg: Springer-Verlag.

Liferov, P., & Bonnemaire, B. (2005). Ice rubble behaviour and strength: Part I. Review of testing and interpretation of results. *Cold Regions Science and Technology*, *41*, 135–151. https://doi.org/10.1016/j.coldregions.2004.10.001

Lishman, B., Sammonds, P., & Feltham, D. (2011). A rate and state friction law for saline ice. *Journal of Geophysical Research*, *116*, C5011. https://doi.org/10.1029/2010JC006334

Moon, T., Joughin, I., & Smith, B. (2015). Seasonal to multiyear variability of glacier surface velocity, terminus position, and sea ice/ice mélange in northwest Greenland. *Journal of Geophysical Research: Earth Surface*, *120*, 818–833. https://doi.org/10.1002/2015JF003494

Moon, T., Sutherland, D. A., Carroll, D., Felikson, D., Kehrl, L., & Straneo, F. (2017). Subsurface iceberg melt key to Greenland fjord freshwater budget. *Nature Geoscience*. https://doi.org/10.1038/s41561-017-0018-z

O'Hern, C. S., Silbert, L. E., Liu, A. J., & Nagel, S. R. (2003). Jamming at zero temperature and zero applied stress: The epitome of disorder. *Physical Review E*, *68*, 11306. https://doi.org/10.1103/PhysRevE.68.011306

Olsson, P., & Teitel, S. (2012). Herschel-Bulkley shearing rheology near the athermal jamming transition. *Physical Review Letters*, *109*, 108001. https://doi.org/10.1103/PhysRevLett.109.108001

Peters, I. R., Amundson, J. M., Cassotto, R., Fahnestock, M., Darnell, K. N., Truffer, M., & Zhang, W. W. (2015). Dynamic jamming of iceberg-choked fjords. *Geophysical Research Letters*, *42*, 1122–1129. https://doi.org/10.1002/2014GL062715

Pfeffer, W. T. (2007). A simple mechanism for irreversible tidewater glacier retreat. *Journal of Geophysical Research*, *112*, F03S25. https://doi.org/10.1029/2006JF000590

Post, A., O'Neel, S., Motyka, R. J., & Streveler, G. (2011). A complex relationship between calving glaciers and climate. *Eos Transactions American Geophysical Union*, *92*(37), 305–307. https://doi.org/10.1029/2011EO370001

Rignot, E., & Kanagaratnam, P. (2006). Changes in the velocity structure of the Greenland Ice Sheet. *Science*, *311*(5763), 986–990. https://doi.org/10.1126/science.1121381

Robel, A. A. (2017). Thinning sea ice weakens buttressing force of iceberg mélange and promotes calving. *Nature Communications*, *8*, 14596. https://doi.org/10.1038/ncomms14596

Sukhorukov, S., & Løset, S. (2013). Friction of sea ice on sea ice. *Cold Regions Science and Technology*, *94*, 1–12.

Sulak, D. J., Sutherland, D. A., Enderlin, E. M., Stearns, L. A., & Hamilton, G. S. (2017). Quantification of iceberg properties and distributions in three Greenland fjords using satellite imagery. *Annals of Glaciology*, *58*(74), 92–106. https://doi.org/10.1017/aog.2017.5

Sutherland, D. A., Roth, G. E., Hamilton, G. S., Mernild, S. H., Stearns, L. A., & Straneo, F. (2014). Quantifying flow regimes in a Greenland glacial fjord using iceberg drifters. *Geophysical Research Letters*, *41*, 8411–8420. https://doi.org/10.1002/2014GL062256

Tankeo, M., Richard, P., & Canot, É. (2013). Analytical solutions of the $\mu(I)$-rheology for fully developed granular flows in simple configurations. *Granular Matter*, *15*, 881–891. https://doi.org/10.1007/s10035-013-0447-3

Taylor, Z. J., Gurka, R., Kopp, G. A., & Liberzon, A. (2010). Long-duration time-resolved PIV to study unsteady aerodynamics. *IEEE Transactions on Instrumentation and Measurement*, *59*(12), 3262–3269. https://doi.org/10.1109/TIM.2010.2047149

Truffer, M., & Motyka, R. J. (2016). Where glaciers meet water: Subaqueous melt and its relevance to glaciers in various settings. *Reviews of Geophysics*, *54*, 220–239. https://doi.org/10.1002/2015RG000494

Tuhkuri, J., & Lensu, M. (1997). Ice tank tests on rafting of a broken ice field (*Ship Lab. Rep. rn-218*). Espoo, Finland: Helsinki Univ. of Technol.

Vaňková, I., & Holland, D. M. (2017). A model of icebergs and sea ice in a joint continuum framework. *Journal of Geophysical Research: Oceans*, *122*, 9110–9125. https://doi.org/10.1002/2017JC013012

van der Veen, C. J. (2013). *Fundamentals of glacier dynamics* (2nd ed.). Boca Raton, FL: CRC Press.

Walter, J. I., Box, J. E., Tulaczyk, S., Brodsky, E. E., Howat, I. M., Ahn, Y., & Brown, A. (2012). Oceanic mechanical forcing of a marine-terminating Greenland glacier. *Annals of Glaciology*, *53*(60), 181–192. https://doi.org/10.3189/2012AoG60A083

Xie, S., Dixon, T. H., Voytenko, D., Dend, F., & Holland, D. M. (2018). Grounding line migration through the calving season of Jakobshavn Isbræ, Greenland, observed with terrestrial radar interferometry. *Cryosphere*, *12*, 1387–1400. https://doi.org/10.5194/tc-2017-231